Supporting Information

Symmetry Dictated Grain Boundary State in a Two-dimensional Topological Insulator

Hyo Won Kim,[†,Δ,] Seoung-Hun Kang,[‡,Δ] Hyun-Jung Kim,[‡,Δ] Kisung Chae,[‡] Suyeon Cho,[#] Wonhee Ko,[†,§] Sangjun Jeon,[‖] Se Hwang Kang,[◊] HeejunYang,[◊] Sung Wng Kim,[◊] Seongjun Park,[†] Sungwoo Hwang,[†] Young-Kyun Kwon,[‡,□] Young-Woo Son[‡,*]*

[†]Samsung Advanced Institute of Technology, Suwon 13595, Korea

[‡]Korea Institute for Advanced Study, Seoul 02455, Korea

[#]Division of Chemical Engineering and Materials Science, Ewha Womans University, Seoul 03760, Korea

[§]Center for Nanophase Materials Sciences, Oak Ridge National Laboratory, Oak Ridge, Tennessee 37831, USA

[‖]Department of Physics, Chung-ang University, Seoul, 06987, Korea

[◊]Department of Energy Science, Sungkyunkwan University, Suwon, 440-746, Korea

[□]Department of Physics and Research Institute for Basic Sciences, Kyung Hee University, Seoul, 02447, Korea

[Δ]H. W. K., S.-H. K. and H. –J. K. contributed equally to this work.

* Correspondence and requests for materials should be addressed to Hyo Won Kim (email: hyowon98.kim@samsung.com) and Young-Woo Son (email: hand@kias.re.kr).

Section I. Dependence on the number of layers of 1T'-$MoTe_2$

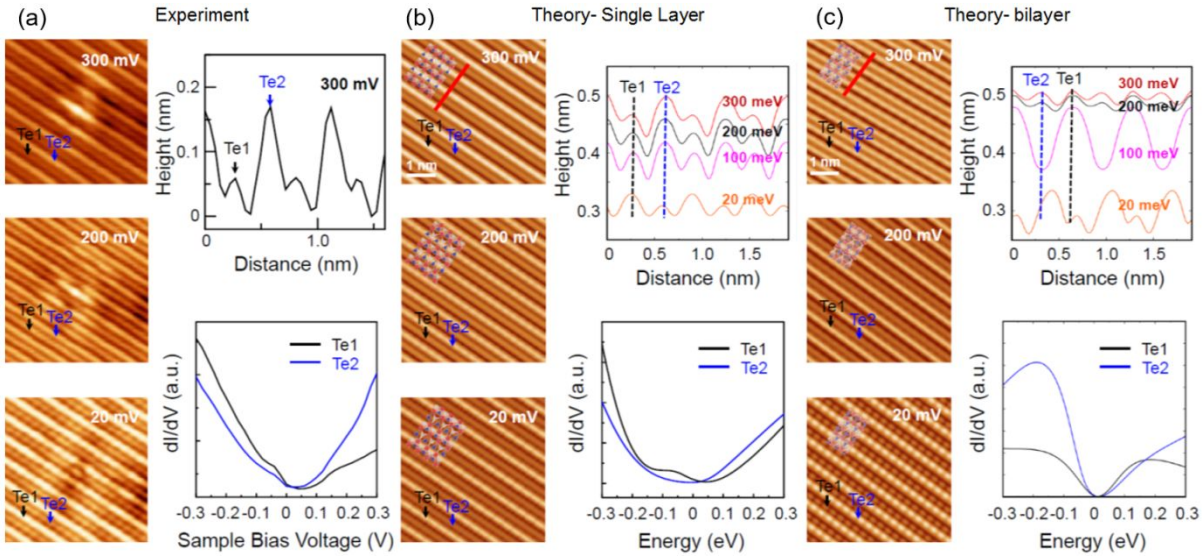

Figure S1. (a) Experimental STM results. (b,c) DFT-calculated results of a single and double layer, respectively. STM images were obtained at 300, 200 and 20 mV for both experiment and calculation.

The experimentally obtained dI/dV spectra of bulk 1T'-$MoTe_2$ are quite similar to those of the simulated single-layer rather than the double-layer. Simulated dI/dV characteristics of the single and double layers of 1T'-$MoTe_2$ and STM heights of Te1 and Te2 rows vary differently depending upon the applied bias voltages as shown in Fig. S1. In the double layer, Te1 is higher than Te2 for all bias voltages of 100, 200 and 300 mV while in experiment and single layer STM and STS simulations those two Te atoms row alternate their topographic heights with increasing bias voltage. Origins of such a bias dependent height alternation is discussed in Section **IV** below.

Section II. Topologically protected metallic state of 1T'-$MoTe_2$.

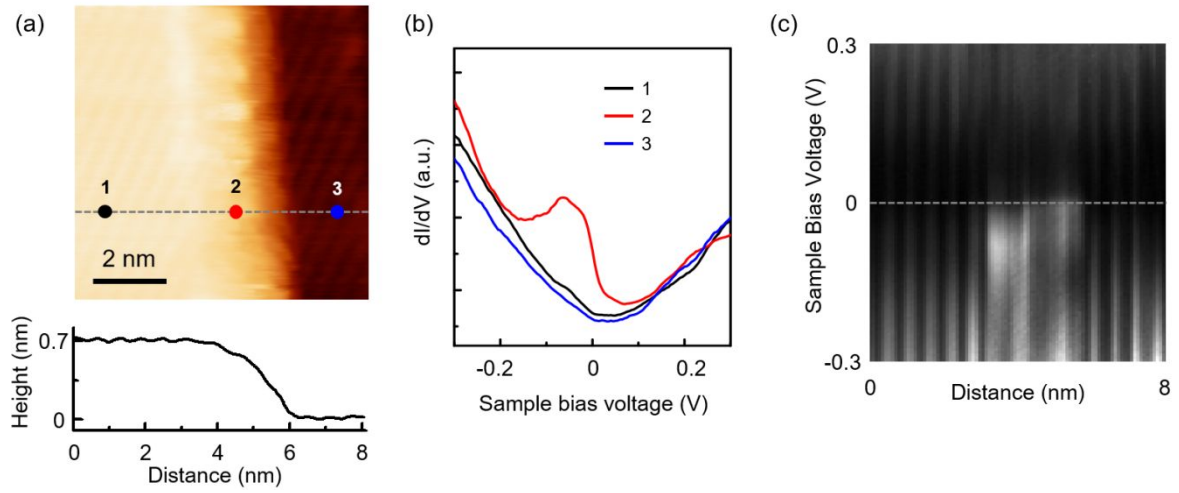

Figure S2. (a) STM topograph of 1T'-$MoTe_2$ (V_s = 0.3 V, I = 0.1 nA) and profile of the height along the dashed gray line. (b) d*I*/d*V* spectra obtained at the positions indicated by black, red and blue dots in (a), respectively. (c) The d*I*/d*V* spectra measured across the step edge of 1T'-$MoTe_2$.

Section III. Effect of the lattice mismatch on the topmost layer and the rest of the sample at the boundaries.

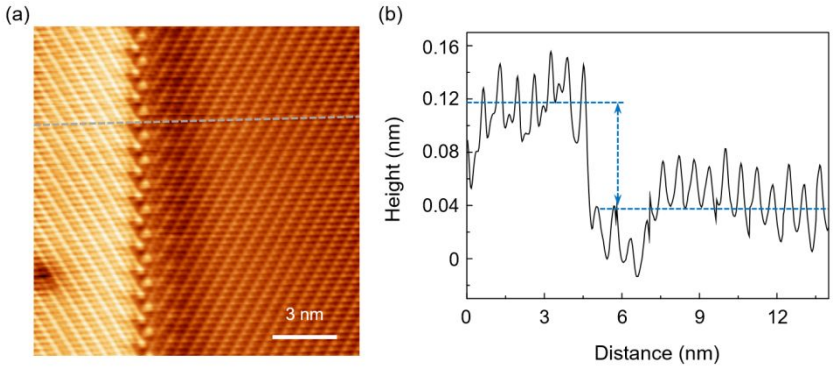

Figure S3. (a) STM topograph of 60° glide reflection boundary (V_s = 0.3 V, I = 0.5 nA). (b) Profile of the height along the dashed gray line in (a). The left side of the domain is lifted up approximately 10 % (80 pm) compared with that of the right side of the domain because of the decreased interlayer coupling due to the inter-layer Te-Te atom stacking configuration.

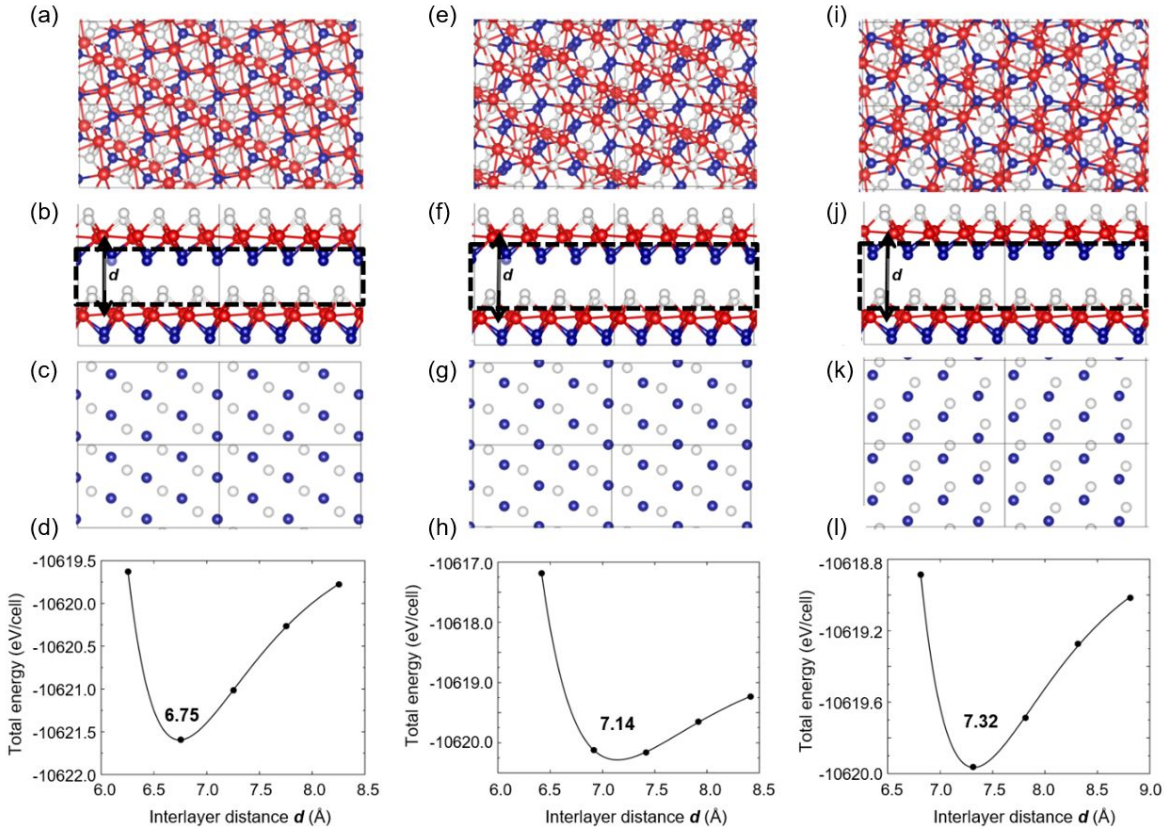

Figure S4. (a,b) Top and side views of atomic structures in bilayer $MoTe_2$ at the T_d bulk phase. (e,f) Top and side views of atomic structures in 60° glide reflection layer on top of the pristine layer. (i,j) Top and side views of atomic structures in 120° two-fold rotation layer on top of the pristine layer. (c,g,k) Top view of inter-layer stacking in the dashed black box at (b,f,j), respectively. (d,h,l) Total energy with respect to interlayer distance *d* in (b,f,j), respectively. The solid black boxes represent the unit cell. As shown here, the interlayer distance increases with a rotation of the upper layer for the formation of grain boundaries.

Section IV. Bias-dependence of STM topographs and d*I*/d*V* maps of 1T'-$MoTe_2$.

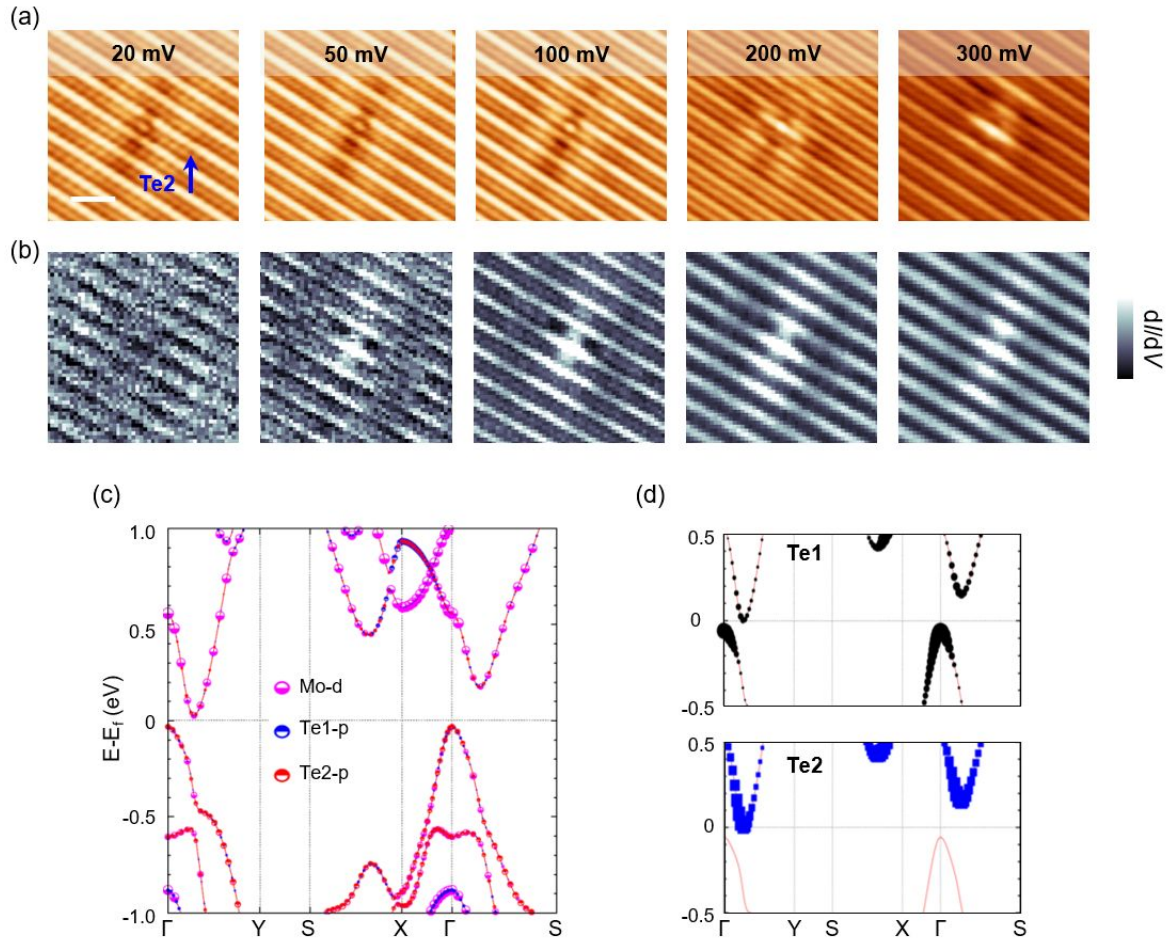

Figure S5. (a) STM topographs and (b) d*I*/d*V* maps for sample bias voltages of V = 20, 50, 100, 200 and 300 mV from left to right panels. A scale bar in the leftist panel is 1nm. The defect in Te2 used as reference. In the STM images obtained at 20, 50 and 100 mV, Te1 row is brighter than Te2 row. At 200 mV the contrast of Te1 and Te2 is similar, and at 300 mV Te2 is brighter than Te1. In the d*I*/d*V* maps at 50, 100, 200 and 300 mV Te2 is brighter than Te1. (c) Band structure of single-layer 1T'-MoTe2, (d) Contributions of Te1 and Te2 *p*-orbitals plotted on the band structure.

Section V. Symmetry and formation energy of grain boundaries

Here, we demonstrate a grain boundary (GB) model to provide atomistic lattice models of the observed GBs. The model provides possible atomic rearrangements at the GB based on coincidence site lattice (CSL) theory and point group analysis, especially when the given crystal is stabilized by lowering its symmetry, e.g., by Jahn-Teller distortion. Instead of constructing a GB directly from the original crystal which has lower symmetry, we generate GB models in a two-step process. Firstly, we create a bi-crystal separated by a symmetric tilt GB from a high-symmetry intermediate crystal by using the CSL theory. The intermediate crystal can be found by searching for the best-matched-fit molecular geometry from the original crystal with the lower symmetry [1]. Subsequently, the intermediate crystals in each domain are distorted back to the original crystal.

In the case of a monolayer of $MoTe_2$, a distorted octahedral motif in a T' phase can be best-matched to the regular octahedron with a point group symmetry of -3 (or six-fold improper rotation: S_6 in Schoenflies notation), and the space group of the crystal is changed from $P2_1/m$ (no. 11) phase to P-3m1 (no. 164) called as T phase as shown in Figure S4a,b. In addition to the improper rotation, there are three additional two-fold rotation axes perpendicular to the improper rotation axis and three vertical mirror planes (Figure S4c). This indicates that a GB, with relative angle of rotation (2θ) of 60º, will create a C_{2y}-symmetric interface with the GB angle of π-2θ, i.e., 120º (Figure S5). Similarly, a 2θ of 120º results in M_y-symmetric interface with the GB angle of 60º (Figure S6). The above also hold when fractional translation is followed, and both of the "symmorphic" and "non-symmorphic" GBs are energetically degenerated prior to the distortion. Once the distortion is considered as indicated by the arrows in Figure S5,S6, the energies of the symmorphic and non-symmorphic GBs become different, and the four GB models of Figure 2b–e are constructed. Since each of the models is tractable by GB operations by which one side of the bi-crystal can be mapped onto the other, we label each of the GB models as follows: 60° mirror $\{M_y|\mathbf{0}\}$, 60° glide-reflection $\{M_y|\frac{1}{2}\mathbf{t}\}$, 120° two-fold rotation $\{C_{2y}|\mathbf{0}\}$ and 120° screw $\{C_{2y}|\frac{1}{2}\mathbf{t}\}$, respectively.

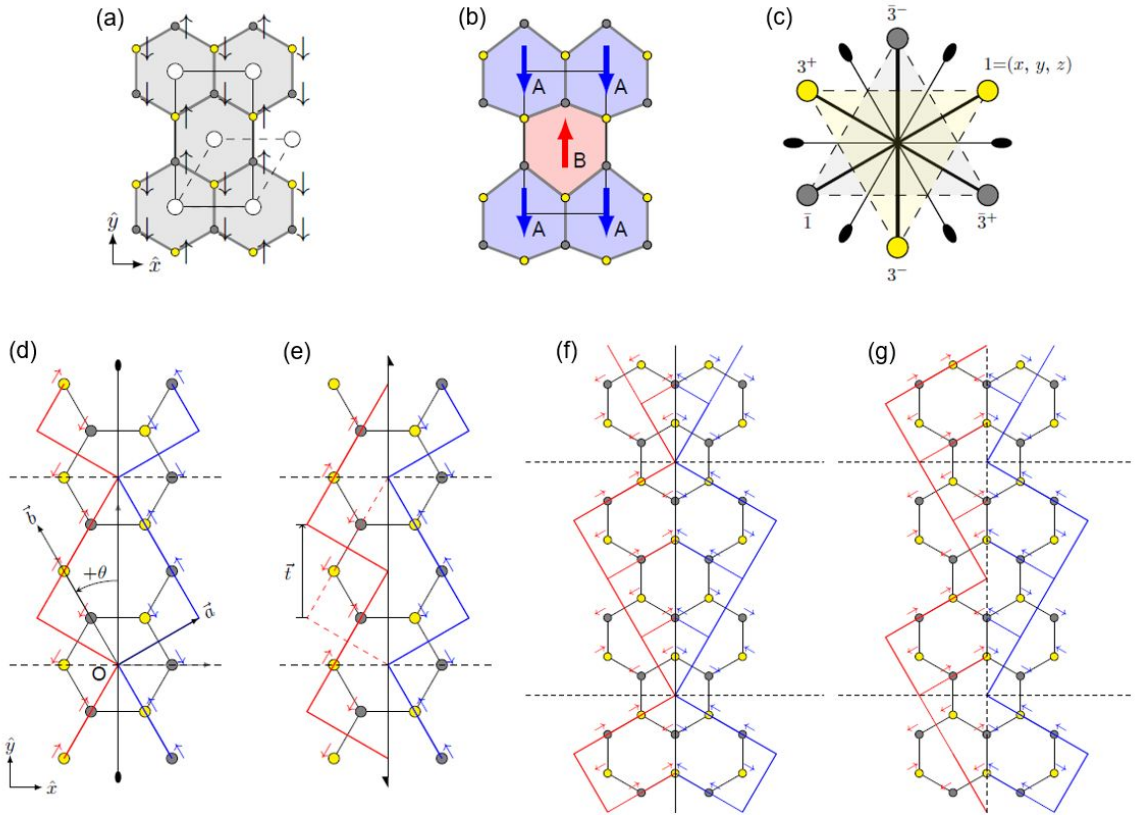

Figure S6. Atomic structures of the $MoTe_2$ crystal in (a) T (P-3m1) and (b) T' ($P2_1/m$) phases. The large white balls represent Mo atoms, and Te atoms are marked as the smaller balls. A phase transition from T to T' phase is indicated by the arrows along $\pm y$ directions next to the Te atoms. The primitive unit cell for the T phase is shown in dashed lines in (a). (c) A point group element of -3. There exist three dyads (two-fold rotation axes) along one of the edges of the triangles shaded in grey and yellow, and three mirror lines (thick lines) dissecting one of the edges. Structural units near the two-fold symmetric grain boundaries with (d) symmorphic and (e) non-symmorphic symmetries. The arrows here indicate the direction of distortion from 1T to 1T' phases. Structural units near the mirror-symmetric grain boundaries with (f) symmorphic and (g) non-symmorphic symmetries. The arrows here indicate the direction of distortion from 1T to 1T' phases.

Section VI. Differential conductance maps

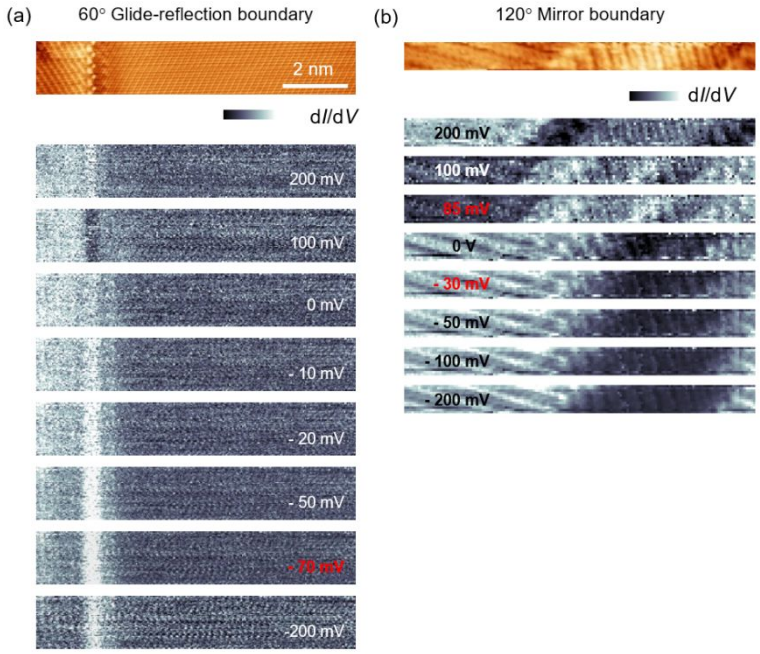

Figure S7. Differential conductance maps. (a) STM topograph and d*I*/d*V* maps of 60º glide-reflection boundary for bias voltages of V = 200, 100, 0, –10, –20, –50, 70 and –200 mV from top to bottom panels. (b). STM topograph and d*I*/d*V* maps of 120º mirror boundary for bias voltages of V = 200, 100, 85, 0, –30, –50, –100 and –200 mV from top to bottom panels.

Section VII. Quasi-particle interference (QPI) acquired along the 60º glide-reflection boundary and 2 nm away from the boundary.

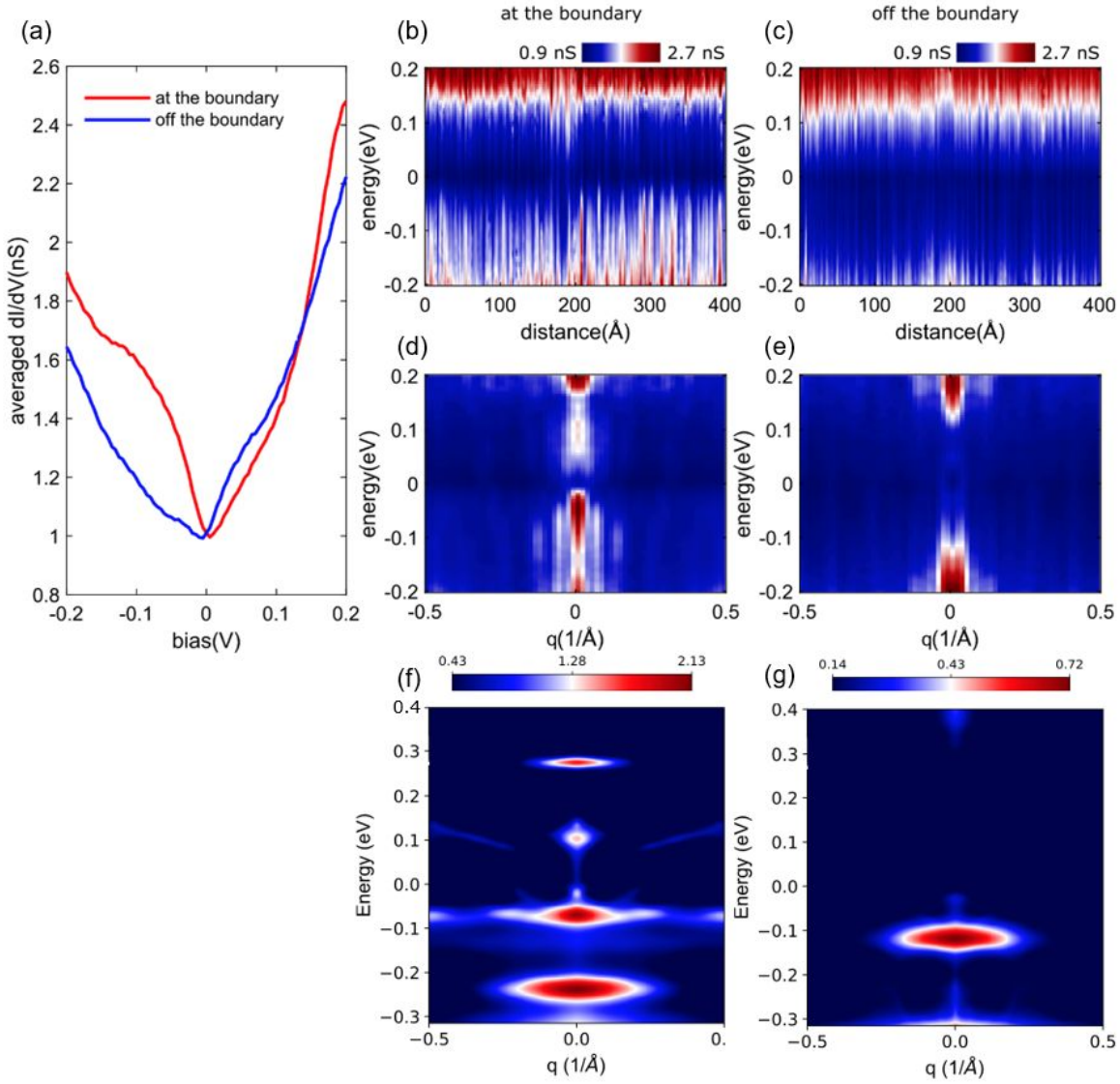

Figure S8. (a) Averaged dI/dV acquired on the boundary (red curve) and 2nm away from the boundary (blue). (b) Spatially resolved dI/dV spectra acquired along the boundary (V_{set} = 0.5 V, I_{set} = 1.5 nA, V_{mod} = 5 mV). (c) Spatially resolved dI/dV spectra acquired parallel to the boundary at 2nm away from the boundary. (V_{set} = 0.5 V, I_{set} = 1.5 nA, V_{mod} = 5 mV). (d,e) Quasiparticle Interference (QPI) data calculated from the dI/dV spectra in (b,e), respectively. (f,g) Simulated QPI data at and away from the boundary, respectively.

To elaborate on the topological nature of the edge mode on the 60° glide-reflection boundary, we have carried out the QPI measurements along the boundaries. The QPI data acquired on the

boundary show strong signals with short $\vec{q}(=\overrightarrow{k_2}-\overrightarrow{k_1})$ vectors between -160 mV and +160 mV (Fig. S8(d)) while the QPI data measured parallel to the boundary at 2 nm away from it shows gap-like feature between -100 mV and +100 mV (Figure S8e). As we discussed in the main text, the 60º glide-reflection boundary has the hourglass type 1D metallic bands due to the non-symmorphic symmetry, while the states away from the boundary have an insulating gap (see Figure 4c in the main text). The spin degeneracy of the 1D bands is lifted by the spin-orbit coupling and as a result, the backscattering interference between $\vec{k}$ and $-\vec{k}$ is prohibited. Moreover, the spin of each band is highly non-parallel due to the spin-momentum locking in this material. Thus, the only allowed scatterings are originated from the states with short momentum differences (small $\vec{q}$ vectors). Although our measurements do not show a strong QPI signal, this weak QPI feature is consistent with the simulated QPI with grain boundary in Figure S8f,g, respectively.

Section VIII. DFT-calculated DOS of Te atoms at 120° two-fold rotation boundary

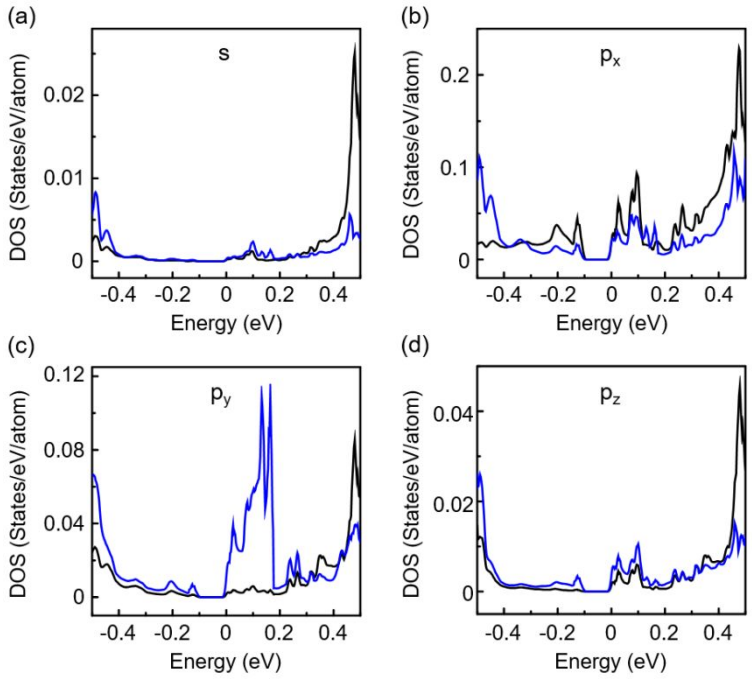

Figure S9. DFT-calculated DOS projected on s, p_x, p_y and p_z orbitals of Te atoms at 120° two-fold rotation boundary.

Section IX. Effects of metallic substrates on GBs

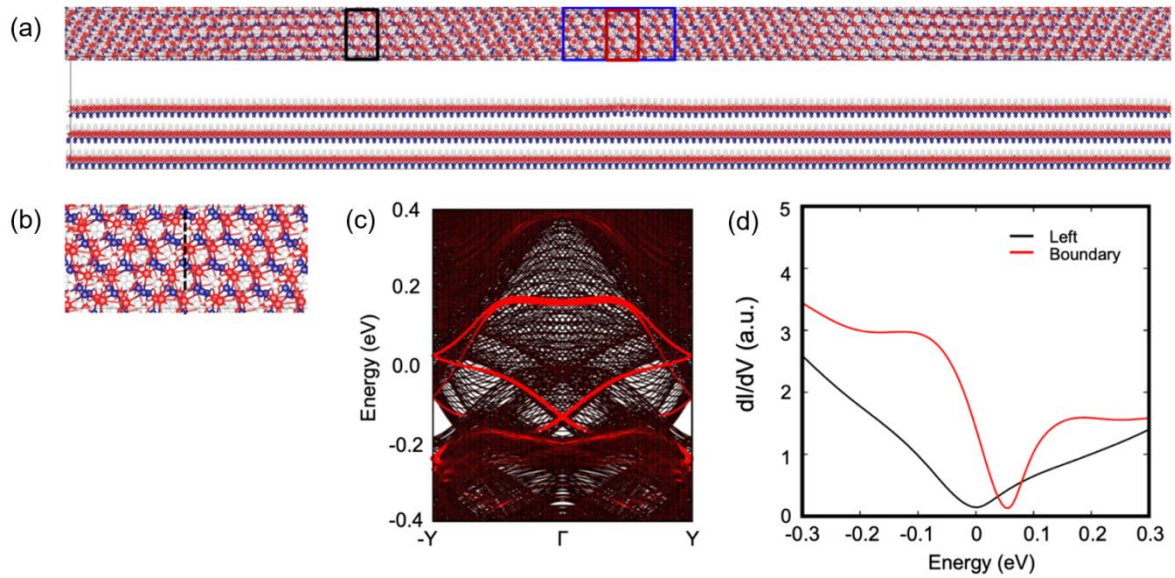

Figure S10. (a) Atomic structures of three layers. The enlarged view of blue box is in (b) and non-symmorphic grain boundary (GB) is denoted by black dotted line. Here, to simulate metallic substrate, we set the on-site Coulomb interaction for Mo atoms for the first and second layer to be 5 eV while the last one is zero. (c) Band structures of (a). The projected bands on the GB are denoted by red lines. (d) The simulated dI/dV spectra on grain boundary (red box in (a)) and bulk (black box in (a)).

Section X. Tight-binding model for 1T'-$MoTe_2$

To investigate the electronic properties of the grain boundaries, we construct a Slater-Koster type TB model which successfully reproduces the DFT based band structure for monolayer 1T'-$MoTe_2$ near the Fermi level. We assume five *d*-orbitals per Mo atom and a *s*-, and three *p*-orbitals per Te atom. The tight-binding Hamiltonian H in the real space is given as,

$$H = \sum_{<i,j>} \sum_{\sigma\alpha\alpha'} \left[t_{i,j}^{\alpha\alpha'} c_{i\alpha\sigma}^{\dagger} c_{j\alpha'\sigma} + \text{H.c.} \right] + H_{SOC},$$

where i, j denotes index for atoms, α, α' for orbitals, and σ for spins, $c_{j\alpha'\sigma}$ is an electron annihilation operatore and $t_{ij}^{\alpha\alpha'}$ is a transfer matrix, which can be parameterized depending on the direction and distance between a pair of orbitals through the Slater-Koster formula.[2] The H_{SOC} represents the Hamiltonian for the on-site SOC,

$$H_{SOC} = -\lambda_{Mo}\hat{S} \cdot \hat{L}_{Mo} + -\lambda_{Te}\hat{S} \cdot \hat{L}_{Te},$$

Where $\lambda_{Mo(Te)}$ is the SOC parameters for Mo (Te) atom, $\hat{S}$ is the spin 1/2 operator, and $\hat{L}_{Mo(Te)}$ is the angular momentum operator of the Mo (Te) atom, respectively [3]. TB parameters obtain by fitting of minimizing the fitness function F,

$$\mathrm{F} = \sum_{n,k} \omega_{n\boldsymbol{k}} (E_{TB}^{n\boldsymbol{k}} - E_{DFT}^{n\boldsymbol{k}})^2,$$

where $\omega_{n\boldsymbol{k}}$ is the weight for the n-th eigenvalue at $\boldsymbol{k}$-point, and $E_{TB(DFT)}^{n\boldsymbol{k}}$ is the eigenvalue obtained by TB (DFT) for monolayer 1T'-$MoTe_2$. We use a nonlinear least-squares method based on the Levenberg-Marquardt algorithm.[4, 5] Using this procedure, we successfully match the DFT band structure and its topological properties as well as the DFT orbital character for 1T'-$MoTe_2$.

References

(1) Banadaki, A. D.; Patala, S. A three-dimensional polyhedral unit model for grain boundary structure in fcc metals. *npj Comput. Mater.* **2017,** 3 (1), 13.

(2) Slater, J. C.; Koster, G. F. Simplified LCAO method for the periodic potential problem. *Phys. Rev.* **1954,** 94 (6), 1498.

(3) Pearce, A. J.; Mariani, E.; Burkard, G. Tight-binding approach to strain and curvature in monolayer transition-metal dichalcogenides. *Phys. Rev. B* **2016,** 94 (15), 155416.

(4) Levenberg, K. A method for the solution of certain non-linear problems in least squares. *Quart. Appl. Math.* **1944,** 2, 164.

(5) Marquardt, D. W. An Algorithm for least-squares estimation of nonlinear parameters. *SIAM J. Appl. Math.* **1963,** 11, 432.